2

Periodically Forced Natural Convection Through the Roof of an Attic-Shaped Building

Suvash Chandra Saha
School of Engineering and Physical Sciences, James Cook University
Australia

1. Introduction

Buoyancy-induced fluid motions in cavities have been discussed widely because of the applications in nature and engineering. A large body of literature exists on the forms of internal and external forcing, various geometry shapes and temporal conditions (steady or unsteady) of the resulting flows. Especially for the classic cases of rectangular, cylindrical or other regular geometries, many authors have investigated imposed temperature or boundary heat fluxes. Reviews of these research can be found in Ostrach (1988) and Hyun (1994). The rectangular cavity is not an adequate model for many geophysical situations where a variable (or sloping) geometry has a significant effect on the system. However, the convective flows in triangular shaped enclosures have received less attention than those in rectangular geometries, even though the topic has been of interest for more than two decades

Heat transfer through an attic space into or out of buildings is an important issue for attic shaped houses in both hot and cold climates. The heat transfer through attics is mainly governed by a natural convection process, and affected by a number of factors including the geometry, the interior structure and the insulation etc. One of the important objectives for design and construction of houses is to provide thermal comfort for occupants. In the present energy-conscious society, it is also a requirement for houses to be energy efficient, i.e. the energy consumption for heating or air-conditioning of houses must be minimized. A small number of publications are devoted to laminar natural convection in two dimensional isosceles triangular cavities in the vast literature on convection heat transfer.

The temperature and flow patterns, local wall heat fluxes and mean heat flux were measured experimentally by Flack (1980; 1979) in isosceles triangular cavities with three different aspect ratios. The cavities, filled with air, were heated/cooled from the base and cooled/heated from the sloping walls covering a wide range of Rayleigh numbers. For the case of heated bottom surface it was found that the flow remained laminar for the low Rayleigh numbers. However, as the Rayleigh number increased, the flow eventually became turbulent. The author also reported the critical Rayleigh numbers of the transition from laminar to turbulent regimes. Kent (2009a) has also investigated the natural convection in an attic space for two different boundary conditions similar to Flack (1980; 1979). The author observed that for top heating and bottom cooling case the flow is dominated by pure conduction and remains stable for higher Rayleigh numbers considered. However, the flow becomes unstable for sufficiently large Rayleigh number for the second case (top cooling and bottom heating).

A comparison study is performed by Ridouane et al. (2005) where the authors compare their numerical results produced for two different boundary conditions, (a) cold base and hot inclined walls (b) hot base and cold inclined walls with the experimental results obtained by Flack (1980; 1979). A good agreement has been obtained between the numerical predictions and the experimental measurements of Nusselt number. A numerical study of above mentioned two boundary conditions has also performed by Ridouane et al. (2006). However, the authors cut a significant portion of bottom tips and applied adiabatic boundary condition there. It is revealed from the analysis that the presence of insulated sidewalls, even of very small height, provides a huge gain of energy and helps keep the attic at the desired temperature with a minimum energy.

The attic problem under the night-time conditions was again investigated experimentally by Poulikakos & Bejan (1983a). In their study, the authors modelled the enclosure as a right-angled triangle with an adiabatic vertical wall, which corresponded to the half of the full attic domain. A fundamental study of the fluid dynamics inside an attic-shaped triangular enclosure subject to the night-time conditions was performed by Poulikakos & Bejan (1983b) with an assumption that the flow was symmetric about the centre plane. Del Campo et al. (1988) examined the entire isosceles triangular cavities for seven possible combinations of hot wall, cold wall and insulated wall using the finite element method based on a stream function or vorticity formulation. A two dimensional right triangular cavity filled with air and water with various aspect ratios and Rayleigh numbers are also examined by Salmun (1995a).

The stability of the reported single-cell steady state solution was re-examined by Salmun (1995b) who applied the same procedures developed by Farrow & Patterson (1993) for analysing the stability of a basic flow solution in a wedge-shaped geometry. Later Asan & Namli (2001) carried out an investigation to examine the details of the transition from a single cell to multi cellular structures. Haese & Teubner (2002) investigated the phenomenon for a large-scale triangular enclosure for night-time or winter day conditions with the effect of ventilation.

Holtzmann et al. (2000) modelled the buoyant airflow in isosceles triangular cavities with a heated bottom base and symmetrically cooled top sides for the aspect ratios of $0.2, 0.5$, and 1.0 with various Rayleigh numbers. They conducted flow visualization studies with smoke injected into the cavity. The main objective of their research was to validate the existence of the numerical prediction of the symmetry-breaking bifurcation of the heated air currents that arise with gradual increments in Rayleigh number. Ridouane & Campo (2006) has also investigated the numerical prediction of the symmetry-breaking bifurcation. The author reported that as Ra is gradually increased, the symmetric plume breaks down and fades away. Thereafter, a subcritical pitchfork bifurcation is created giving rise to an asymmetric plume occurring at a critical Rayleigh number, $Ra = 1.42 \times 10^5$. The steady state laminar natural convection in right triangular and quarter circular enclosures is investigated by Kent et al. (2007) for the case of winter-day temperature condition. A number of aspect ratios and Rayleigh numbers have been chosen to analyse the flow field and the heat transfer.

Unlike night-time conditions, the attic space problem under day-time (heating from above) conditions has received very limited attention. This may due to the fact that the flow structure in the attics subject to the daytime condition is relatively simple. The flow visualization experiments of Flack (1979) showed that the daytime flow remained stable and laminar for all the tested Rayleigh numbers (up to about 5×10^6). Akinsete & Coleman (1982) numerically simulated the attic space with hot upper sloping wall and cooled base. Their aim was to

obtain previously unavailable heat transfer data relevant to air conditioning calculations. This study considered only half of the domain. For the purpose of air conditioning calculations, Asan & Namli (2000) and Kent (2009b) have also reported numerical results for steady, laminar two-dimensional natural convection in a pitched roof of triangular cross-section under the summer day (day-time) boundary conditions.

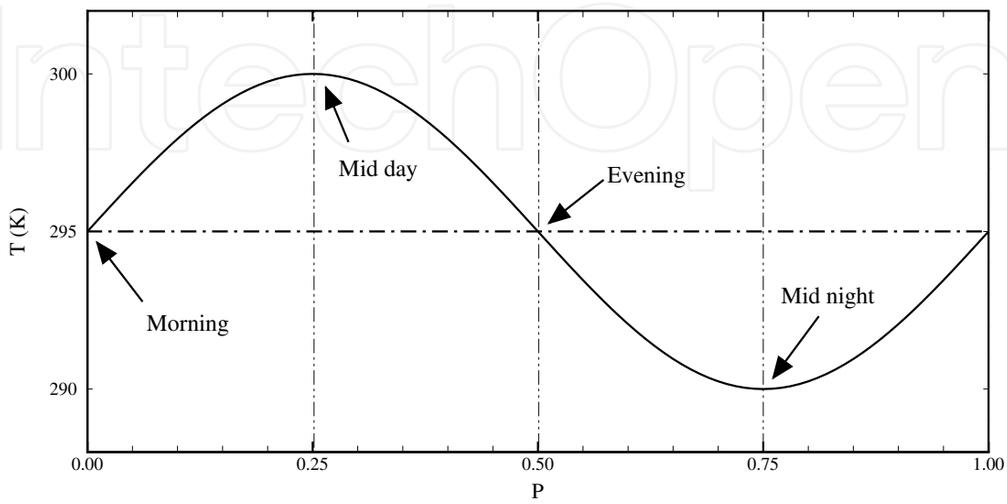

Fig. 1. Temperature boundary condition on the incline walls of the enclosure

Recently, the transient flow development inside the attic space has been analysed by using scaling analysis with numerical verification by (Saha, 2011a;b; Saha et al., 2010a;c; Saha, 2008). The authors considered different types of thermal conditions, such as, sudden heating/cooling and ramp heating/cooling. In real situations, however, the attic space of buildings is subject to alternative heating and cooling over a diurnal cycle as it can be seen in Fig. 1. A very few studies for diurnal heating and cooling effect on the attic space are reported in the literature (Saha et al., 2010b; 2007). The authors discussed a general flow structure and heat transfer due to the effect of periodic thermal forcing. A detailed explanation of choosing the period for the model attic is required as the 24-hour period for the field situation is not applicable here.

In this study, numerical simulations of natural convection in an attic space subject to diurnal temperature condition on the sloping wall have been carried out. An explanation of choosing the period of periodic thermal effect has been given with help of the scaling analysis which is available in the literature. Moreover, the effects of the aspect ratio and Rayleigh number on the fluid flow and heat transfer have been discussed in details as well as the formation of a pitchfork bifurcation of the flow at the symmetric line of the enclosure.

2. Formulation of the problem

The physical system is sketched in Fig. 2, which is an air-filled isosceles triangular cavity of variable aspect ratios. Here $2l$ is the length of the base or ceiling, T_0 is the temperature applied on the base, T_A is the amplitude of temperature fluctuation on the inclined surfaces, h is the height of the enclosure and P is the period of the thermal forcing.

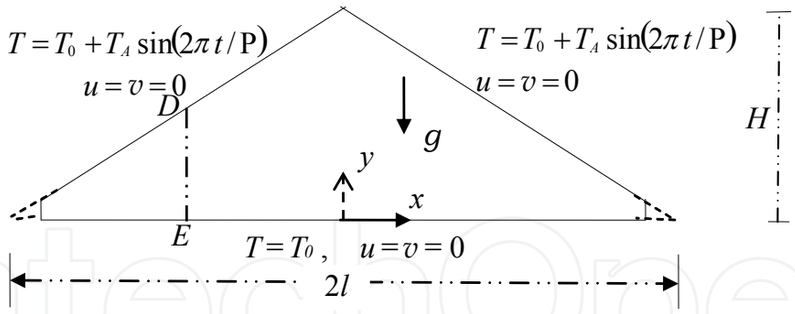

Fig. 2. A schematic of the geometry and boundary conditions of the enclosure

Under the Boussinesq approximations the governing continuity, momentum and energy equations take the following forms.

$$\frac{\partial u}{\partial x} + \frac{\partial v}{\partial y} = 0 \tag{1}$$

$$\frac{\partial u}{\partial t} + u\frac{\partial u}{\partial x} + v\frac{\partial u}{\partial y} = -\frac{1}{\rho}\frac{\partial p}{\partial x} + \nu\left(\frac{\partial^2 u}{\partial x^2} + \frac{\partial^2 u}{\partial y^2}\right) \tag{2}$$

$$\frac{\partial v}{\partial t} + u\frac{\partial v}{\partial x} + v\frac{\partial v}{\partial y} = -\frac{1}{\rho}\frac{\partial p}{\partial y} + \nu\left(\frac{\partial^2 v}{\partial x^2} + \frac{\partial^2 v}{\partial y^2}\right) + g\beta\left(T - T_0\right) \tag{3}$$

$$\frac{\partial T}{\partial t} + u\frac{\partial T}{\partial x} + v\frac{\partial T}{\partial y} = \kappa\left(\frac{\partial^2 T}{\partial x^2} + \frac{\partial^2 T}{\partial y^2}\right) \tag{4}$$

where u and v are the velocity components along $x-$ and $y-$directions, t is the time, p is the pressure, ν, ρ, β and κ are kinematic viscosity, density of the fluid, coefficient of thermal expansion and thermal diffusivity respectively, g is the acceleration due to gravity and T is the fluid temperature.

The boundary conditions for the present numerical simulations are also shown in Fig. 2. Here, the temperature of the bottom wall of the cavity is fixed at $T = T_0$. A periodic temperature boundary condition is applied to the two inclined walls. The Rayleigh number for the periodic boundary condition has been defined based on the maximum temperature difference between the inclined surface and the bottom over a cycle as

$$Ra = \frac{2g\beta T_A h^3}{\kappa\nu}$$

Three aspect ratios 0.2, 0.5 and 1.0, four Rayleigh numbers, 1.5×10^6, 7.2×10^5, 1.5×10^4, and 1.5×10^3, and a fixed Prandtl number 0.72 are considered in the present investigation. Based on the experimental observations of Flack (1979), which reported the critical Rayleigh number for the flow to become turbulent, we have chosen the maximum Rayleigh number, $Ra = 1.5 \times 10^6$ so that the flow stays in the laminar regime. It is understood that in real situations the Rayleigh number may be much higher than this and an appropriate turbulence model should be applied. This is beyond the scope of this study. In order to avoid the singularities at the tips in the numerical simulation, the tips are cut off by 5% and at the cutting points (refer to Fig. 2) rigid non-slip and adiabatic vertical walls are assumed. We anticipate that this modification of the geometry will not alter the overall flow development significantly.

3. Selection of the physical period

The period is determined in consideration of the scaling predictions of Saha et al. (2010a;b;c) which have demonstrated that the time for the adjustment of the temperature in the thermal boundary layer is by far shorter than the thermal forcing period of 24 hours in field situations. For sudden heating/cooling boundary conditions the steady state time scale for the boundary layer development from Saha et al. (2010c) is

$$t_s = \frac{(1+Pr)^{1/2}(1+A^2)^{1/2}}{ARa^{1/2}Pr^{1/2}}\left(\frac{h^2}{\kappa}\right), \tag{5}$$

and the heating-up or cooling-down time scale for the enclosure to be filled with hot or cold fluid under the same boundary conditions as in Saha et al. (2010c) is

$$t_f = \frac{(1+Pr)^{1/4}}{A^{1/2}Ra^{1/4}Pr^{1/4}(1+A^2)^{1/4}}\left(\frac{h^2}{\kappa}\right), \quad \text{for} \quad t_f > t_s \tag{6}$$

On the other hand, the quasi-steady time scale for ramp heating/cooling boundary condition of the boundary layer development for the case when the ramp time is longer than the quasi-steady time is (see Saha et al., 2010c)

$$t_{sr} = \frac{(1+Pr)^{1/3}(1+A^2)^{1/3}}{A^{2/3}Ra^{1/3}Pr^{1/3}}\left(\frac{t_p}{h^2/\kappa}\right)^{1/3}\left(\frac{h^2}{\kappa}\right), \tag{7}$$

and the heating-up or cooling-down time scale of the enclosure under the same boundary conditions from Saha et al. (2010a) is

$$t_{fr} = \frac{\left[h(1+A^2)^{1/2} - Ax_1\right]^2}{A^{1/2}\kappa Ra^{1/4}(1+A^2)^{5/4}}, \tag{8}$$

where x_1 is given by

$$x_1 \sim L\left[1 - \left(1 - \frac{\kappa A^{1/2}Ra^{1/4}(1+A^2)^{1/4}}{h^2}t_p\right)^{1/2}\right], \tag{9}$$

However, if the cavity is filled with cold fluid before the ramp is finished then the filling up time is given in Saha et al. (2010a) as

$$t_{fq} \sim \frac{h^{8/7}t_p^{3/7}}{\kappa^{4/7}Ra^{1/7}A^{2/7}(1+A^2)^{1/7}}, \tag{10}$$

Table 1 presents the scaling values of the steady and quasi-steady times for sudden and ramp heating/cooling boundary conditions respectively for different A and Ra. The highest Rayleigh number considered here for three different aspect ratio is $Ra = 1.5 \times 10^6$. It is noticed that the steady state times for the boundary layer for this Rayleigh number of $A = 0.2, 0.5$ and 1.0 are $8.1s$, $2.54s$ and $2.26s$ respectively. However, for the lowest Rayleigh number, $Ra = 7.2 \times 10^3$ the steady state time for $A = 0.5$ is $35.76s$. On the other hand, the quasi-steady time for the ramp temperature boundary condition depends on the length of the ramp. If we assume the ramp time to be $1000s$ then the quasi-steady times for these aspect ratios are $40.51s$, $18.62s$ and $17.23s$ respectively and for the lowest Rayleigh number, $Ra = 7.2 \times 10^3$

Aspect ratio	Steady state time (t_s) for sudden heating/cooling		Quasi-steady time (t_{sr}) for ramp heating/cooling (t_p = 1000s)	
	$Ra = 1.5\times10^6$	$Ra = 7.2\times10^3$	$Ra = 1.5\times10^6$	$Ra = 7.2\times10^3$
A=0.2	8.15s	-	40.51s	-
A=0.5	2.54s	35.76s	18.62s	108.53s
A=1.0	2.26s	-	17.23s	-

Table 1. Steady state and quasi-steady times for sudden and ramp boundary conditions respectively for different A and Ra.

the quasi-steady time for the aspect ratio $A = 0.5$ is $108.53s$ which is much shorter than the ramp time ($1000s$). If the ramp time is $200s$ the quasi-steady time of $A = 0.5$ for the lowest Rayleigh number considered here is $63.47s$. Still the quasi-steady time is about half of the ramp time. Therefore, what happened between the quasi-steady time and the ramp time is, once the quasi-steady state time t_{sr} is reached, the boundary layer stops growing according to $\kappa^{1/2}t^{1/2}$ which is only valid for conductive boundary layers. The thermal boundary layer is in a quasi-steady mode with convection balancing conduction. Further increase of the heat input simply accelerates the flow to maintain the proper thermal balance. The thickness and the velocity scales during this quasi-steady mode is (see Saha et al., 2010c)

$$\delta_T \sim \frac{h(1+A^2)^{1/4}}{Ra^{1/4}A^{1/2}}\left(\frac{t_p}{t}\right)^{1/4}. \tag{11}$$

and

$$u \sim Ra^{1/2}\frac{\kappa}{h}\left(\frac{t}{t_p}\right)^{1/2}. \tag{12}$$

respectively. When the hot fluid travels through the boundary layer and reaches the top tip of the cavity then it has no choice but to move downward along the symmetry line of the cavity. In this way the cavity is filled up with hot fluid with a horizontal stratification of the thermal field. However, during the cooling phase, the boundary layer is not stable for the Rayleigh numbers considered here. In that case initially a cold boundary layer develops adjacent to the inclined wall which is potentially unstable to the Rayleigh Bénard instability, which may manifest in a form of sinking plumes. These plumes mix up the cold fluid with the hot fluid inside the cavity until the end of the cooling phase.

Moreover, Table 2 shows the scaling values of the filling-up times for sudden and ramp heating/cooling boundary conditions for different A and Ra. It is seen that the heating-up or cooling-down times for the sudden heating/cooling boundary condition for $A = 0.5$ and $Ra = 1.5 \times 10^6$ is $42.39s$ and for $Ra = 7.2 \times 10^3$ and the same aspect ratio is $159.01s$. For aspect ratios 0.2 and 1.0 the filling-up times are $83.24s$ and $31.61s$ respectively when $Ra = 1.5 \times 10^6$. The filling-up times for ramp heating/cooling boundary conditions for $A = 0.5$ are $145.07s$ and $308.77s$ when $Ra = 1.5 \times 10^6$ and 7.2×10^3 respectively and $t_p = 1000s$. For two other aspect ratios, $A = 0.2$ and 1.0, the filling-up times are $213.32s$ and $122.67s$ respectively for $Ra = 1 \times 10^6$. However, the filling-up time for ramp boundary conditions depends on the length of the ramp time. If the ramp time is $200s$ then the filling-up time for the lowest

Aspect ratio	Filling-up time (t_f) for sudden heating/cooling		Filling-up time (t_{fr}) for ramp heating/cooling (t_p = 1000s)	
	$Ra = 1.5\times10^6$	$Ra = 7.2\times10^3$	$Ra = 1.5\times10^6$	$Ra = 7.2\times10^3$
A=0.2	83.24s	-	213.32s	-
A=0.5	42.39s	159.01s	145.07s	308.77s
A=1.0	31.61s	-	122.67s	-

Table 2. Heating-up/cooling-down times for sudden and ramp boundary conditions respectively for different A and Ra.

Rayleigh number considered here is 154.90s for $A = 0.5$. These times are very short when compared to the thermal forcing period of 24 hours in field situations. Therefore, the period of the thermal cycle may be considered as 400s or more based on the above discussions for the following numerical simulations. However, for a better understanding of the flow at in the quasi-steady mode, we have chosen a thermal forcing period of 2000s for all the simulations.

4. Numerical scheme and grid and time step dependence tests

Equations (1) - (4) are solved along with the initial and boundary conditions using the SIMPLE scheme. The finite volume method has been chosen to discretize the governing equations, with the QUICK scheme (see Leonard & Mokhtari, 1990) approximating the advection term. The diffusion terms are discretized using central-differencing with second order accurate. A second order implicit time-marching scheme has also been used for the unsteady term. An extensive mesh and time step dependence tests have been coonducted in Saha et al. (2010a;b;c)

5. Flow response to the periodic thermal forcing

The flow response to the periodic thermal forcing and the heat transfer through the sloping boundary are discussed for the case with $A = 0.5$, $Pr = 0.72$ and $Ra = 1.5 \times 10^6$ in this section.

5.1 General flow response to diurnal heating and cooling

Since the initial flow is assumed to be isothermal and motionless, there is a start-up process of the flow response. In order to minimize the start-up effect, three full thermal forcing cycles are calculated in the numerical simulation before consideration of the flow. It is found that the start-up effect for the present case is almost negligible, and the flow response in the third cycle is identical to that in the previous cycle. In the following discussion, the results of the third cycle are presented.

Fig. 3 shows snapshots of streamlines and the corresponding isotherms and vector field at different stages of the cycle. The flow and temperature structures, shown in Fig. 3 at $t = 2.00P$, represent those at the beginning of the daytime heating process in the third thermal forcing cycle. At this time, the inclined surfaces and the bottom surface of the enclosure have the same temperature, but the temperature inside the enclosure is lower than the temperature on the boundaries due to the cooling effect in the previous thermal cycle. The residual temperature structure, which is formed in the previous cooling phase, is still present at $t = 2.00P$. The

corresponding streamline contours at the same time show two circulating cells, and the temperature contours indicate stratification in the upper and lower section of the enclosure with two cold regions in the centre.

As the upper surface temperature increases further, a distinct temperature stratification is established throughout the enclosure by the time $t = 2.05P$ (see Fig. 3). The streamlines at this stage indicate that the centers of the two circulating cells have shifted closer to the inclined surfaces, indicating a strong conduction effect near those boundaries. This phenomenon has been reported previously in Akinsete & Coleman (1982) and Asan & Namli (2000) for the daytime condition with constant heating at the upper surface or constant cooling at the bottom surface.

At $t = 2.25P$, the temperature on the inclined surfaces peaks. Subsequently, the temperature drops, representing a decreasing heating effect. Since the interior flow is stably stratified prior to $t = 2.25P$, the decrease of the temperature at the inclined surface results in a cooling event, appearing first at the top corner and expanding downwards as the surface temperature drops further. At $t = 2.45P$, two additional circulating cells have formed in the upper region of the enclosure, and the newly formed cells push the existing cells downwards. The corresponding temperature contours show two distinct regions, an expanding upper region responding to the cooling effect, and a shrinking lower region with stratification responding to the decreasing heating effect. By the time $t = 2.50P$, the daytime heating ceases; the lower stratified flow region has disappeared completely and the flow in the enclosure is dominated by the cooling effect. At this time, the top and the bottom surfaces again have the same temperature, but the interior temperature is higher than that on the boundaries.

As the upper inclined surface temperature drops below the bottom surface temperature ($t = 2.70P$, Fig. 3), the cold-air layer under the inclined surfaces becomes unstable. At the same time, the hot-air layer above the bottom surface also becomes unstable. As a consequence, sinking cold-air plumes and rising hot-air plumes are visible in the isotherm contours and a cellular flow pattern is formed in the corresponding stream function contours. It is also noticeable that the flow is symmetric about the geometric symmetry plane at this time. However, as time increases the flow becomes asymmetric about the symmetric line (see isotherms at $t = 2.95P$). The large cell from the right hand side of the centreline, which is still growing, pushes the cell on the left of it towards the left tip. At the same time this large cell also changes its position and attempts to cross the centreline of the cavity and a small cell next to it moves into its position and grows.

At $t = 2.975P$, the large cell in the stream lines has crossed the centerline and the cell on the right of it grows and becomes as large as it is after a short time (for brevity figures not included). The flow is also asymmetric at this time. However, it returns to a symmetric flow at the time $t = 3.00P$ which is the same as that at $t = 2.00P$, and similar temperature and flow structures to those at the beginning of the forcing cycle are formed. The above described flow development is repeated in the next cycle.

The horizontal velocity profiles (velocity parallel to the bottom surface) and the corresponding temperature profiles evaluated along the line DE shown in Fig. 2 at different time instances of the third thermal forcing cycle are depicted in Fig. 4. At the beginning of the cycle ($t = 2.00P$) the velocity is the highest near the roof of the attic (see Fig. 4a), which is the surface driving the flow. At the same time, the body of fluid residing outside the top wall layer moves fast toward the bottom tips to fill up the gap. As time progresses the vertical velocity increases and the horizontal temperature decreases (see $t = 2.05P$). A three layer structure in the velocity field

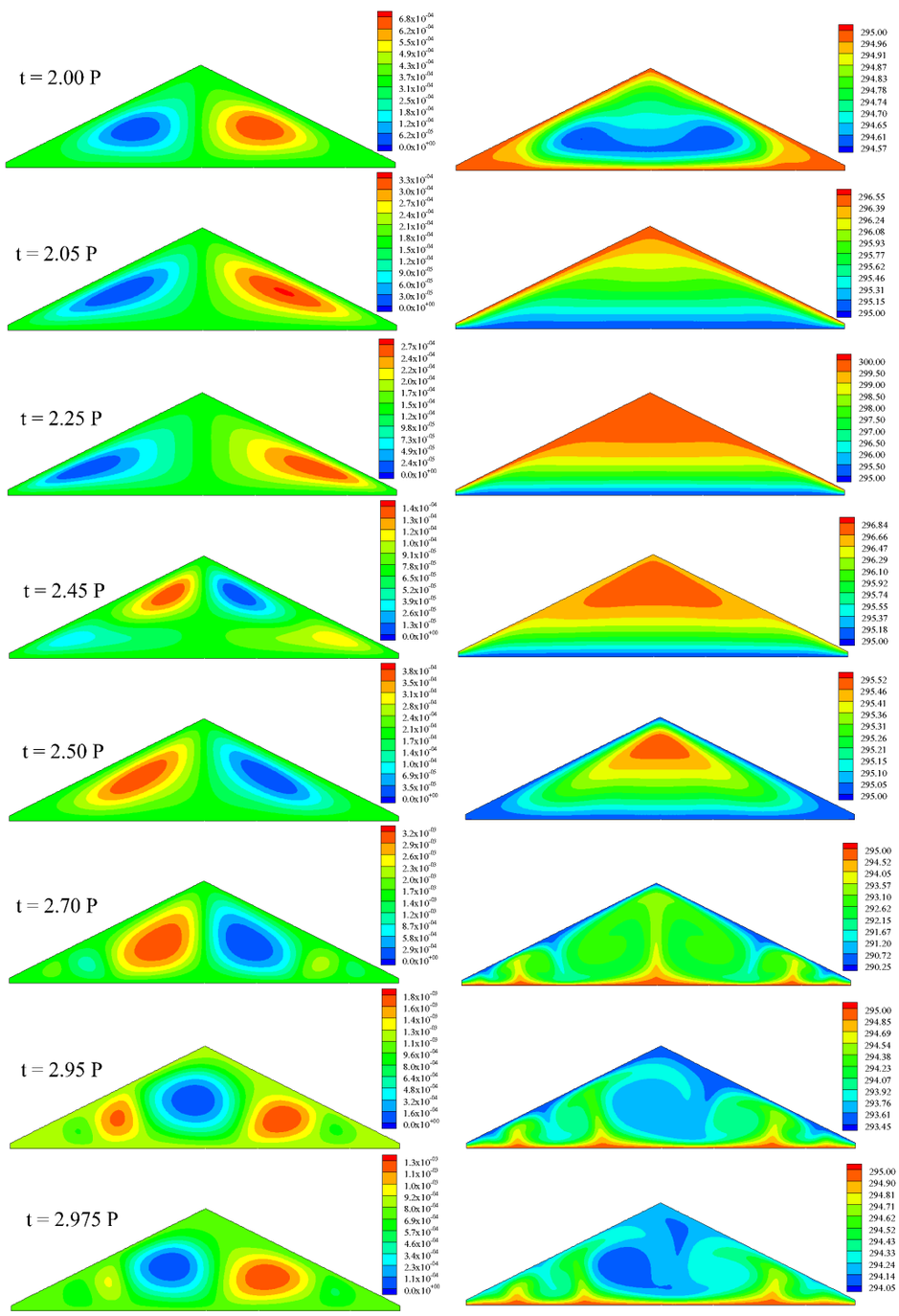

Fig. 3. A series of snapshots of stream function and temperature contours of the third cycle at different times for $A = 0.5$ and $Ra = 1.5 \times 10^6$. Left: streamlines; right: isotherms.

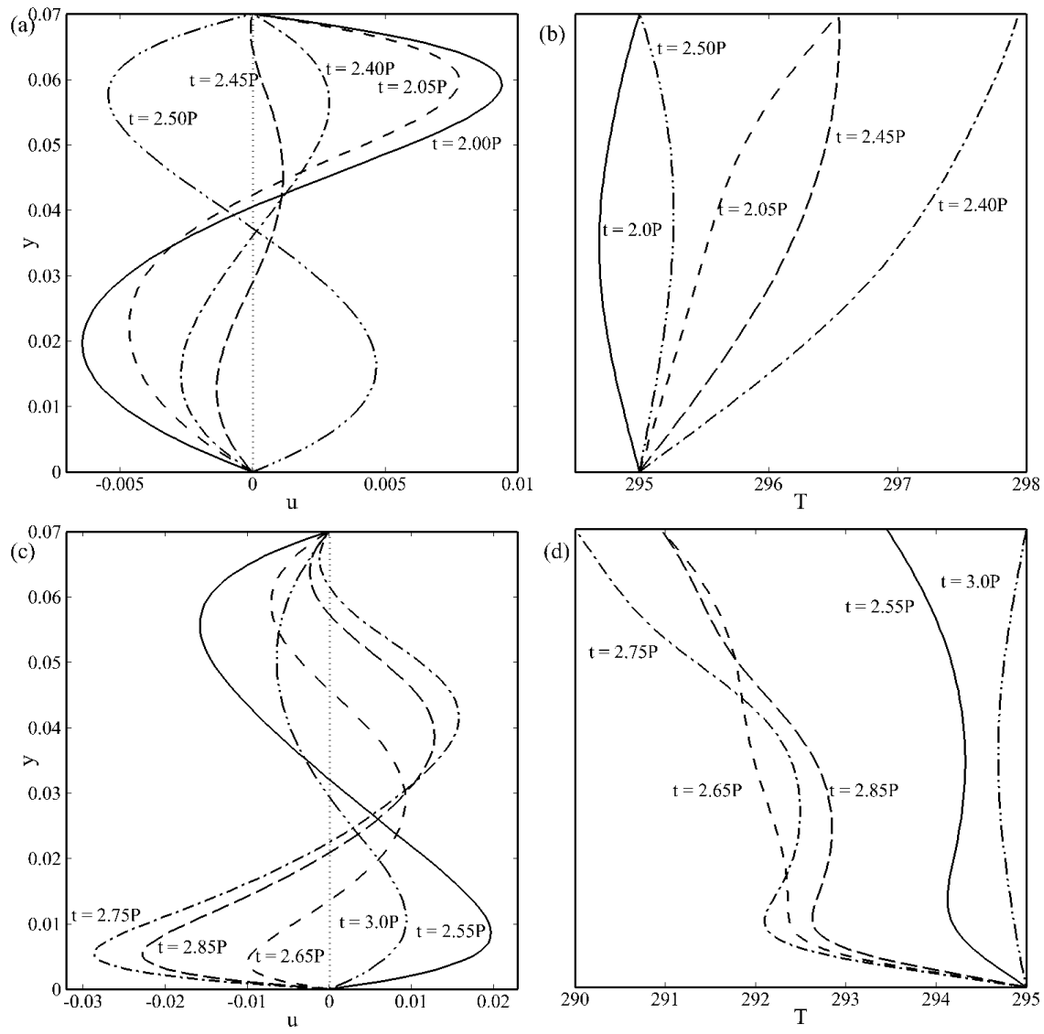

Fig. 4. Horizontal velocity profile (left) and temperature profile (right) along DE for $A = 0.5$ with $Ra = 1.5 \times 10^6$.

is found at $t = 2.45P$. At this time the top portion of the cavity is locally cooled and the bottom portion is still hot (see Fig. 3). After that time the flow completely reverses at $t = 2.50P$. It is noted that at this time the horizontal velocity is lower than that at the beginning of the cycle despite that the temperatures on the sloping boundary and the ceiling are the same at both times (see Fig. 4b). This is due to the fact that at the beginning of the cycle the flow is mainly dominated by convection as a result of the cooling effect in the second half of the previous thermal cycle. However, the flow is dominated by conduction at $t = 2.50P$ as a result of the heating effect in the first half of the current thermal cycle.

As mentioned above, at the beginning of the cycle ($t = 2.00P$) the temperatures on the horizontal and inclined surfaces are the same as shown in Fig. 4(b). However the temperature near the mid point of the profile line is lower than that at the surfaces by approximately $0.5K$, which is consistent with the previous discussion of the flow field. Subsequently the temperature of the top surface increases ($t = 2.05P$) while the bottom surface temperature

remains the same. It is noteworthy that the top surface reaches its peak temperature at $t = 2.25P$ (for brevity the profile is not included). After this time the top surface temperature starts to decrease which can be seen at time $t = 2.40P$. By comparing the temperature profiles at $t = 2.05P$ and $t = 2.45P$ shown in Fig. 4(b), it is clear that the temperatures at both the top and bottom surfaces are the same for these two time instances. However, different temperature structures are seen in the interior region. The same phenomenon has been found at the times $t = 2.50P$ and $t = 2.00P$.

In Fig. 4(c), the velocity profiles at the same location during the night-time cooling phase are displayed. In this phase the flow structure is more complicated. At $t = 2.55P$ the velocity near the bottom surface is slightly higher than that near the top. Again a three layer structure of the velocity field appeared which is seen at $t = 2.65P, 2.75P$ and $2.85P$. The maximum velocity near the ceiling occurs at $t = 2.75P$ when the cooling is at its maximum. After that it decreases and the flow reverses completely at $t = 3.0P$. The corresponding temperature profiles for the night-time condition are shown in Fig. 4(d). It is seen that the temperature lines are not as smooth as those observed for the daytime condition. At $t = 2.55P$, the temperature near the bottom surface decreases first and then increases slowly with the height and again decreases near the inclined surface. This behaviour near the bottom surface is due to the presence of a rising plume. Similar behaviour has been seen for $t = 2.75P$ and $2.85P$. However, at $t = 2.65P$ it decreases slowly after rapidly decreasing near the bottom surface. At $t = 3.00P$ again the bottom and top surface temperatures are the same with a lower temperature in the interior region.

5.2 Heat transfer across the attic

The Nusselt number, which has practical significance, is calculated as follows:

$$Nu = \frac{h_{\text{eff}} h}{k} \tag{13}$$

where the heat transfer coefficient heff is defined by

$$h_{\text{eff}} = \frac{q}{T_A} \tag{14}$$

Here q is the convective heat flux through a boundary. Since the bottom surface temperature is fixed at $295K$ and the sloping wall surface temperature cycles between 290K and 300K (refer to Figure 1), a zero temperature difference between the surfaces occurs twice in a cycle. Therefore, the amplitude of the temperature fluctuation (T_A) is chosen for calculating the heat transfer coefficient instead of a changing temperature difference, which would give an undefined value of the heat transfer coefficient at particular times.

Fig. 5 shows the calculated average Nusselt number on the inclined and bottom surfaces of the cavity. The time histories of the calculated Nusselt number on the inclined surfaces exhibit certain significant features. Firstly, it shows a periodic behaviour in response to the periodic thermal forcing. Secondly within each cycle of the flow response, there is a time period with weak heat transfer and a period with intensive heat transfer. The weak heat transfer corresponds to the daytime condition when the flow is mainly dominated by conduction and the strong heat transfer corresponds to the night-time condition. At night, the boundary layers adjacent to the inclined walls and the bottom are unstable. Therefore, sinking and rising plumes are formed in the inclined and horizontal boundary layers. These plumes dominate

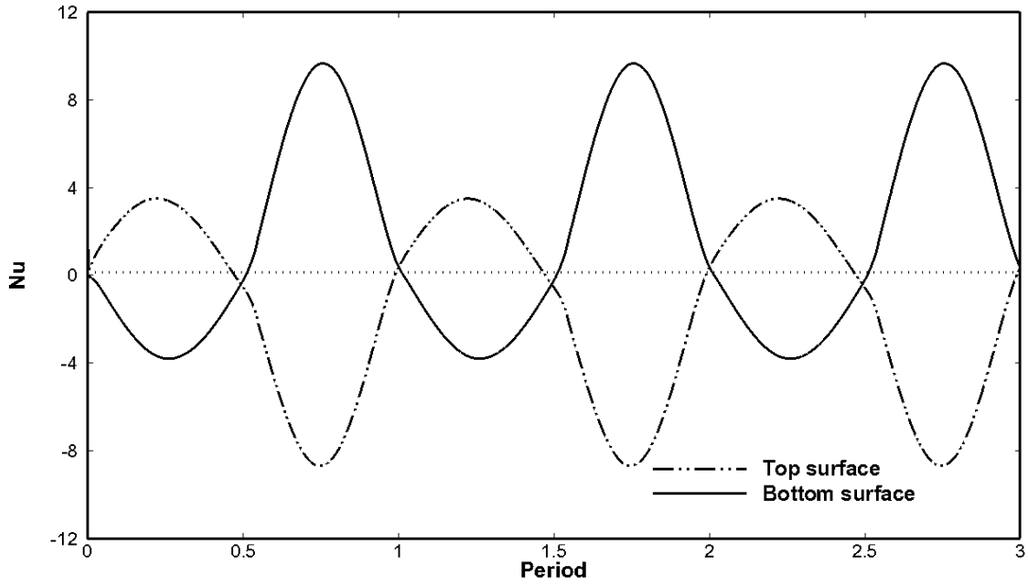

Fig. 5. Average Nusselt number on the top and bottom surfaces of the cavity for three full cycles where $Ra = 1.5 \times 10^6$ and $A = 0.5$

the heat transfer through the sloping walls of the cavity. Finally the calculated maximum Nusselt number on sloping surfaces is 8.72, occurring during the night-time period, whereas the maximum value during the day time is only 3.48, for the selected Rayleigh number and aspect ratio. The corresponding Nusselt number calculated on the bottom surface shows similar behavior as that of top surfaces. Note that the Nusselt number calculated using (13) is based on the total heat flux across the surfaces. Since the surface area of the top surface is larger ($0.595m^2$) than the bottom surface ($0.532m^2$), therefore the total surface heat flux on the top surfaces will be lower than that of the bottom surface. However, the integral of the heat transfer rate for a cycle on both surfaces has been calculated and it is found that both are the same.

5.3 Effects of the aspect ratio on the flow response

The flow responses to the periodic thermal forcing for the other two aspect ratios are shown in Figs. 6 and 7, which are compared with the flow response for $A = 0.5$ shown in Fig. 3. It is found that the aspect ratio of the enclosure has a great influence on the flow response as well as heat transfer. The residual effect of the previous cycle on the current cycle has been found similar for all aspect ratios (see at $t = 2.0P$ in Figs. 3, 6, 7) and the flow and temperature structures during the heating process is qualitatively the same for $A = 1.0$ and $A = 0.2$ as those for $A = 0.5$ for $Ra = 1.5 \times 10^6$. However, during the cooling phase there are significant changes of flow and heat transfer among these aspect ratios. For the night-time the high velocity area of these three aspect ratios exists between the two cells where the stream function gradient is higher. Therefore, the buoyancy drives the warm air upwards from the bottom of the geometry and at the same time the gravitational force acts on the cold air downwards from the top. This upward and downward movement can be seen in the temperature contours as a form of rising and sinking plumes.

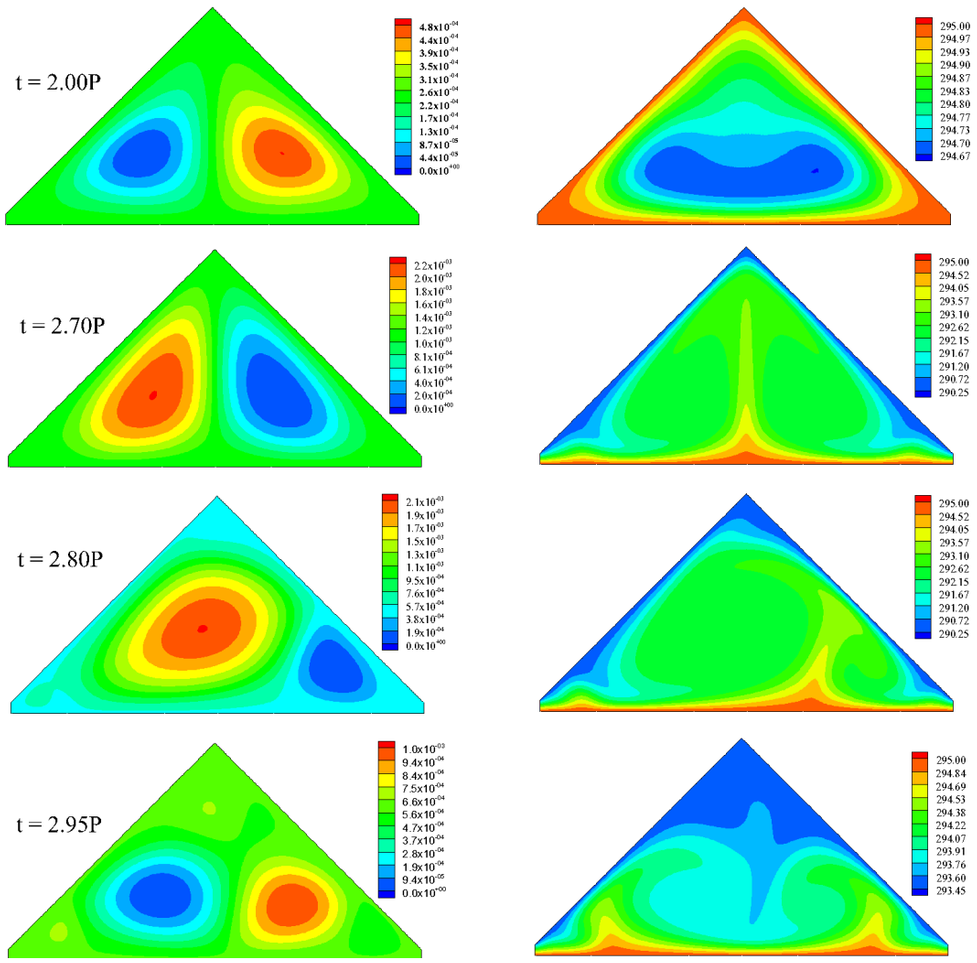

Fig. 6. A series of snapshots of stream function and temperature contours of the third cycle at different times for $A = 1.0$ and $Ra = 1.5 \times 10^6$. Left: streamlines; right: isotherms.

It has been revealed that the flow remains symmetric about the geometrical centreline throughout the cycle for aspect ratio $A = 0.2$, whereas, it is asymmetric during the cooling phase for the other two aspect ratios for $Ra = 1.5 \times 10^6$. It is also anticipated that the asymmetric solution is one of two possible mirror images of the solutions. Another noticeable variation with different aspect ratios is the formation of a circulation cell near the top of the enclosure. It is seen for $A = 1.0$ that there is an extra vortex (Fig. 6 at $t = 2.95P$) on the top of the cavity, which is completely absent for $A = 0.5$ and $A = 0.2$. The flow and temperature fields for the smallest aspect ratio $A = 0.2$ are more complex, with several circulation cells on either side of the central line and many plumes alternately rising and falling throughout the domain, as seen in Fig. 7. These cells and plumes are the result of flow instability described earlier.

Fig. 8 illustrates the horizontal velocity and temperature profiles for aspect ratio $A = 1.0$ along the line DE as shown in Fig. 2 for $Ra = 1.50 \times 10^6$. Since the flow is stable and stratified during the day (the heating phase), the structures of the velocity and temperature profiles are qualitatively the same as those for other aspect ratios.

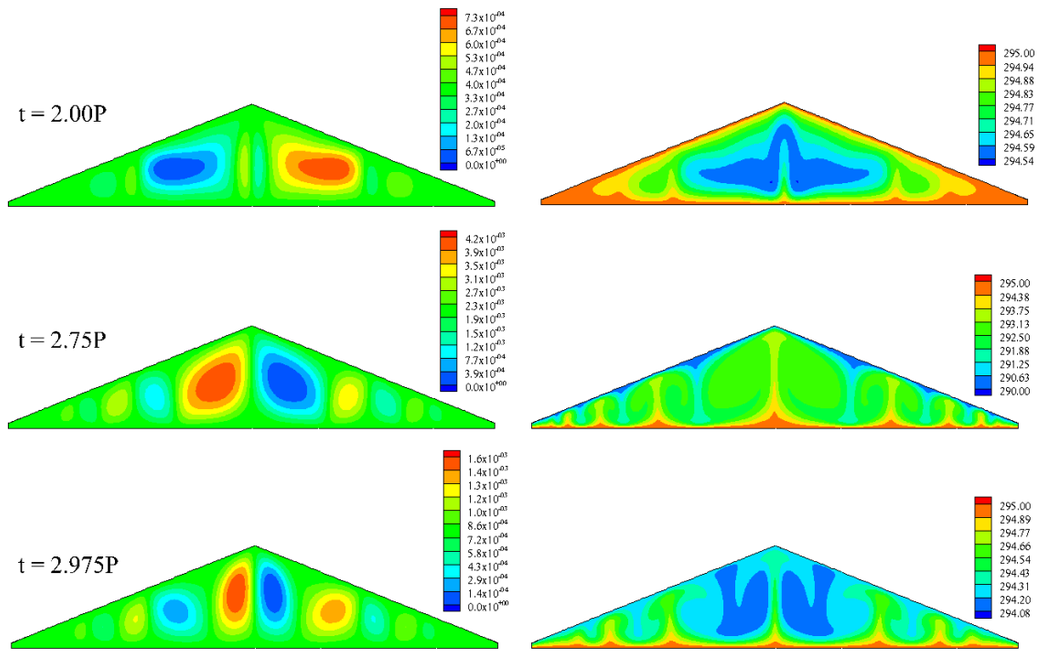

Fig. 7. A series of snapshots of stream function and temperature contours of the third cycle at different times for $A = 0.2$ and $Ra = 1.5 \times 10^6$. Left: streamlines; right: isotherms.

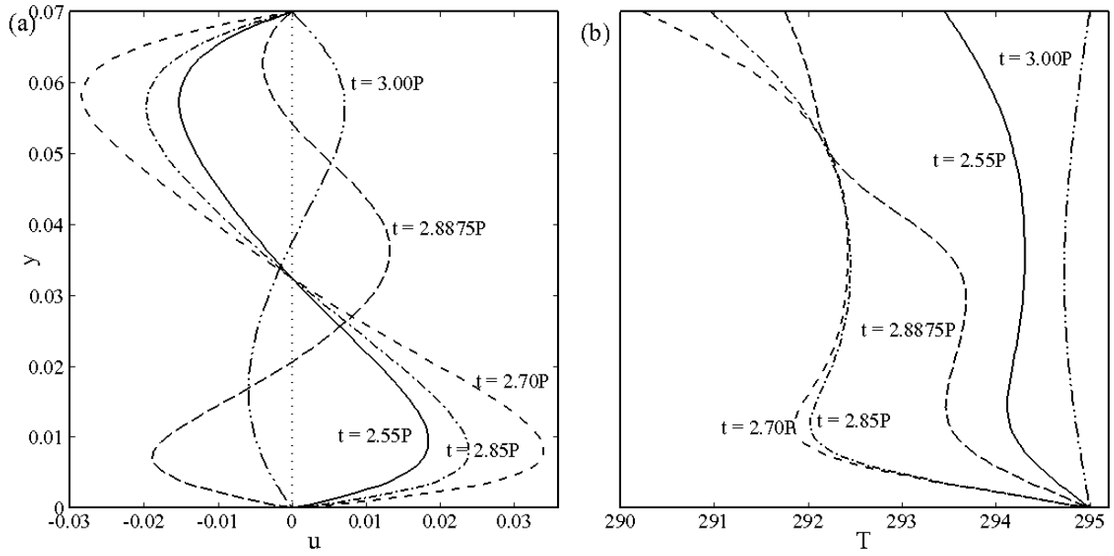

Fig. 8. Horizontal velocity profile (left) and temperature profile (right) along DE for $A = 1.0$ with $Ra = 1.50 \times 10^6$.

At the night-time the velocity and temperature profiles for $A = 1.0$ are more complicated than that for $A = 0.5$. As seen in Fig. 8, at time $t = 2.55P$ when the upper surface temperature is lower than the bottom surface, the velocity near the bottom surface is slightly higher than that near the inclined surfaces. After that the velocity increases near both the surfaces until $t = 2.75P$. Since a plume-type instability dominates the flow during the cooling phase and the flow has an asymmetric behaviour for a certain period of time, the horizontal velocity is in the same direction near both surfaces and is in an opposite direction in the middle (see $t = 2.8875P$). As the flow transits into the next thermal cycle, it becomes very weak. The corresponding temperature contours are plotted in Fig. 8(b). It is seen that the temperature profiles near the bottom surface show a wave shaped for almost the whole cooling phase due to the rising plumes (see Fig. 3). At the time $t = 2.8875P$, when three layers of the velocity structure is seen, the corresponding temperature profile also shows a wave structure.

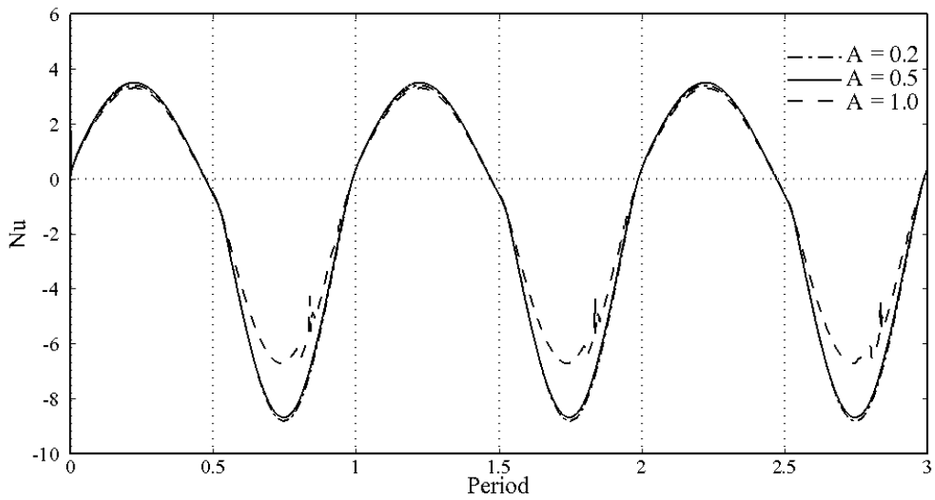

Fig. 9. Comparison of the average Nusselt number of three aspect ratios for $Ra = 1.5 \times 10^6$

Fig. 9 shows the calculated average Nusselt number on the inclined surfaces of the cavity for three different aspect ratios. The time histories of the calculated Nusselt number exhibit certain common features. Within each cycle of the flow response, there is a time period with weak heat transfer and a period with intensive heat transfer for each aspect ratio. The weak heat transfer corresponds to the day time condition when the heat transfer is dominated by conduction and the strong heat transfer corresponds to the night-time condition when convection dominates the flows and the instabilities occur in the form of rising and sinking plumes. During the day time the heat transfer rate is almost the same for all three aspect ratios. However, at the night time the heat transfer rate for $A = 1.0$ is much smaller than that for the other two aspect ratios, and there is a fluctuation of the Nusselt number for a certain period of time. This fluctuation is absent in the other two aspect ratios. This may be due to the fact that less convective cells are present in the streamlines for $A = 1.0$ than those for the other two aspect ratios. Moreover, the movement of the dominating cell for $A = 1.0$ is faster than those for other two. In addition to this, an extra cell appears on the top of the cavity for the aspect ratio $A = 1.0$. It is also noticed that there is not much difference in heat transfer for

the aspect ratios $A = 0.5$ and 0.2. The highest average Nusselt numbers for $A = 1.0, 0.5$ and 0.2 are $6.55, 8.72$ and 8.76 respectively.

5.4 Effects of Rayleigh number on the flow response and heat transfer

Fig.10 shows snapshots of stream function and temperature contours for the aspect ratio 0.5 with three different Rayleigh numbers, $Ra = 1.5 \times 10^6, 7.2 \times 10^4$ and 7.2×10^3. The contours for $Ra = 7.2 \times 10^4$ are qualitatively the same as for $Ra = 1.5 \times 10^6$. It is found that in the heating phase (i.e. when the upper wall temperature is higher than the temperature of the bottom) the flow structures are qualitatively similar for all Rayleigh numbers. However, in the cooling phase the flow behaviour is strongly dependent on the Rayleigh numbers. Stream function and temperature contours are presented at two different times, $t = 2.70P$ and $2.95P$ for each Rayleigh number in Fig. 10. In the isotherms, rising and sinking plumes are visible for $Ra = 1.5 \times 10^6$ and 7.2×10^4 at both times. A cellular flow pattern is seen in the corresponding stream function contours for $Ra = 1.5 \times 10^6$. However, only two convective cells are present for $Ra = 7.2 \times 10^4$. If the Rayleigh number is decreased further ($Ra = 7.2 \times 10^3$), the flow becomes weaker. Only two cells are seen in the stream function contours and the temperature field is horizontally stratified (see the corresponding isotherms). At $t = 2.95P$, the flow seems to be asymmetric along the centre line for $Ra = 1.5 \times 10^6$. However, for the lower Rayleigh numbers the asymmetric behaviour is not visible.

Fig.11 shows the comparison of the Nusselt number among four Rayleigh numbers for a fixed aspect ratio 0.5. It is seen clearly that during the heating phase the heat transfer rate is weaker, whereas it is much stronger in the cooling phase. With the increase of the Rayleigh number, the Nusselt number increases throughout the thermal cycle, but the rate of increase is much higher in the cooling phase compared to that in the heating phase. The maximum Nusselt number in the cooling phase for $Ra = 1.5 \times 10^6$ is about 2.5 times of the maximum Nusselt number during the heating phase. It is noticeable that for the lowest Rayleigh number $Ra = 1.5 \times 10^3$, the heat transfer rate during the heating and cooling phases are almost the same. The maximum Nusselt number for the four different Rayleigh numbers, $Ra = 1.5 \times 10^6, 7.2 \times 10^5, 7.2 \times 10^4$ and 7.2×10^3 for the aspect ratio 0.5 are $8.65, 7.34, 4.26$ and 3.11 respectively.

5.5 Transition between symmetric and asymmetric flows

The highest Rayleigh number considered in this study for the three aspect ratios is 1.5×10^6. Except for $A = 0.2$, the flow in the cavity for the other two aspect ratios is observed to undergo a supercritical pitchfork bifurcation for this Rayleigh number, in which case one of two possible mirror image asymmetric solutions is obtained. This asymmetric behaviour was first reported numerically and experimentally by Holtzmann et al. (2000) in their study of the case of a sudden cooling boundary condition. If the flow is asymmetric, the horizontal velocity along the midplane of the isosceles triangle would be nonzero. Based on this hypothesis, Fig.12 illustrates the absolute value of maximum horizontal velocity along the geometric center line for $A = 1.0$ and 0.5. It is seen in this figure that, for both aspect ratios, the maximum horizontal velocity is zero up to approximately $t = 0.70P$ in each cycle, suggesting that the flow is symmetric during this time. However, after this time the maximum horizontal velocity starts to increase, indicating that the flow becomes asymmetric. The asymmetry remains until shortly before the end of each cycle when the flow returns to symmetric again. The same asymmetric behaviour of the flow is seen for the Rayleigh number 7.2×10^5 for the aspect ratios 0.5 and 1.0.

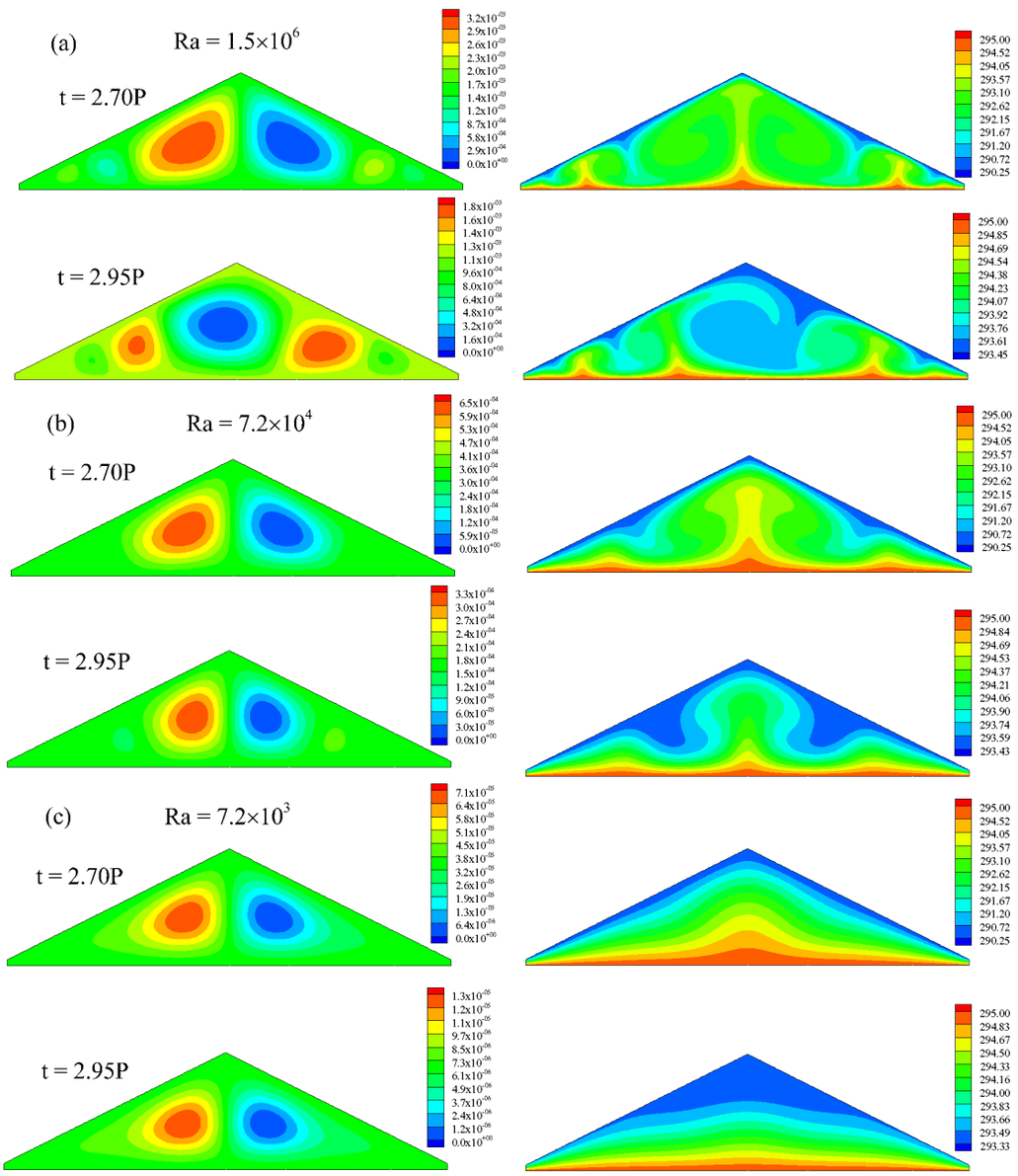

Fig. 10. Snapshots of stream function contours (left) and isotherms (right) of the third cycle at different times and different Rayleigh numbers with fixed $A = 0.5$.

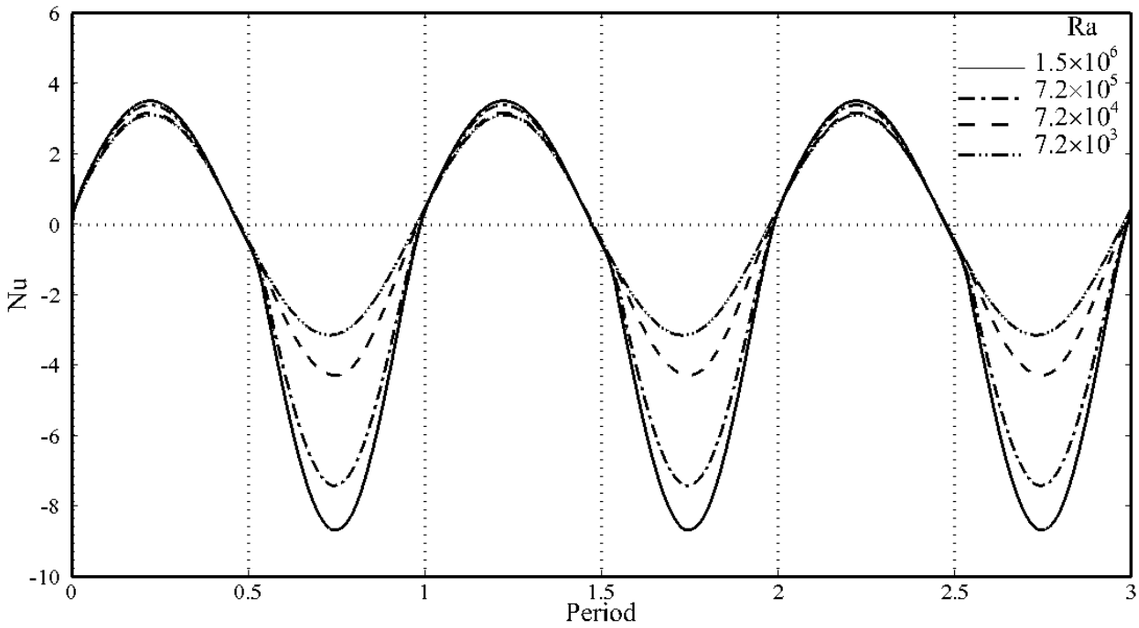

Fig. 11. Comparison of the average Nusselt number of four Rayleigh numbers for $A = 0.5$

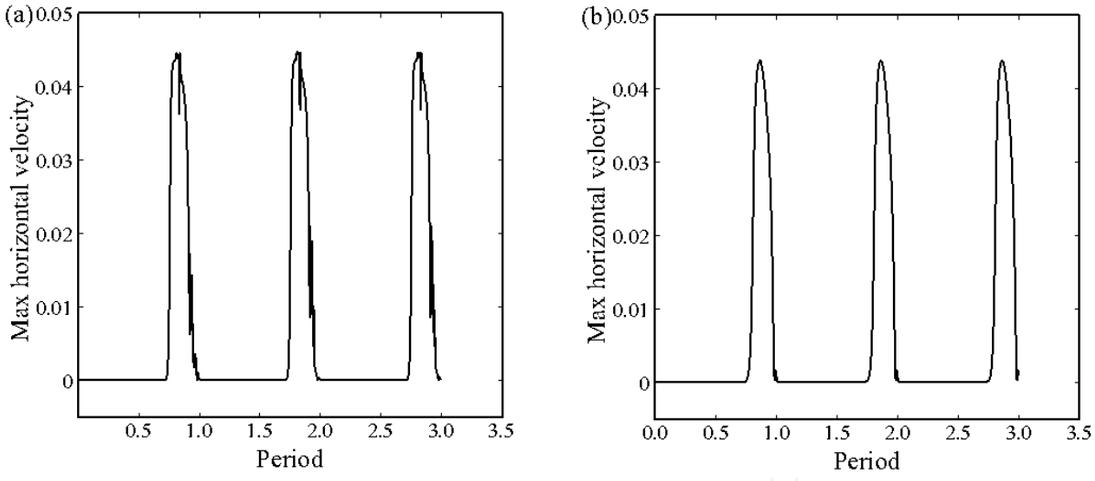

Fig. 12. The maximum horizontal velocity along the symmetry line for (a) $A = 1.0$ and (b) $A = 0.5$ with $Ra = 1.5 \times 10^6$.

The same results have been found when the average Nusselt numbers obtained for both inclined surfaces are compared for the aspect ratios 1.0 and 0.5, which are shown in Fig.13 (a) and (b) respectively. It is seen that at about $t = 0.70P$, the calculated Nusselt numbers at the left and right inclined surfaces start to diverge, but later they meet again before the end of each cycle.

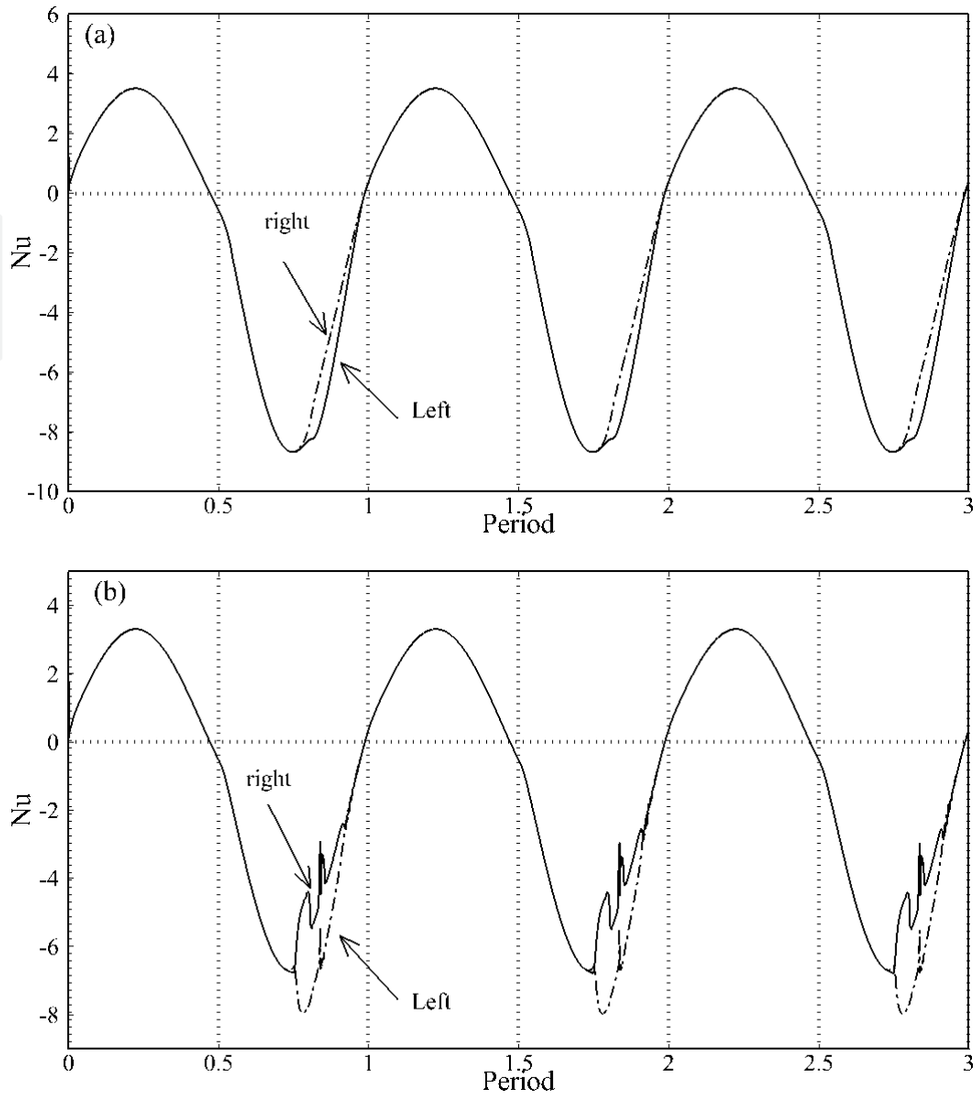

Fig. 13. Comparison of the average Nusselt number on two inclined surfaces of the enclosure for (a) $A = 1.0$ and (b) $A = 0.5$ with $Ra = 1.5 \times 10^6$

6. Conclusions

Natural convection in an attic-shaped building with the effect of periodic thermal forcing has been carried out in this study based on numerical simulations. An attempt has also been taken to predict the period of the model attic using scaling analysis. Three aspect ratios of $A = 1.0, 0.5$ and 0.2 with four Rayleigh numbers of $Ra = 1.5 \times 10^6, 7.2 \times 10^5, 7.2 \times 10^4$ and 7.2×10^3 for each aspect ratio have been considered here. Many important features are revealed from the present numerical simulations. It is found that the flow response to the temperature variation on the external surface is fast, and thus the start-up effect is almost negligible. The occurrence of sinking cold-air plumes and rising hot-air plumes in the isotherm contours and the formation of cellular flow patterns in the stream function contours confirm the presence of the Rayleigh-Bénard type instability. It is also observed that the flow undergoes a transition

between symmetry and asymmetry about the geometric symmetry plane over a diurnal cycle for the aspect ratios of $A = 1.0$ and 0.5 with the Rayleigh numbers 1.5×10^6 and 7.2×10^5. For all other cases the flow remains symmetric. A three-layer velocity structure has been found along the line at DE as shown in Fig. 2 in both the daytime heating phase (due to local cooling effect in the upper sections of the inclined walls) and night-time cooling phase when the flow becomes asymmetric. Furthermore, the flow response in the daytime heating phase is weak, whereas the flow response in the night-time cooling phase, which is dominated by convection, is intensive. At lower Rayleigh numbers the flow becomes weaker for all aspect ratios, and no asymmetric flow behaviour has been noticed.

7. Nomenclature

A	slope of the attic
g	acceleration due to gravity
h	height of the attic
h_{eff}	heat transfer coefficient
K	Kelvin
k	thermal conductivity
l	half horizontal length of the attic
Nu	Nusselt number
p	pressure
P	period of the cycle
Pr	Prandtl number
q	convective heat flux
Ra	Rayleigh number
t	time
T	temperature of the fluid
T_0	temperature of the ambient fluid
T_A	the amplitude
u, v	velocity components along the x- and y- axes respectively
x, y	cartesian coordinates

Greek letters

β	Volumetric coefficient of thermal expansion
ν	Kinematic viscosity
ρ	Density of the fluid
κ	thermal diffusivity
ΔT	temperature difference between the surface and the ambient

8. References

Akinsete, V. A. & Coleman, T. A. (2000). Heat transfer by steady laminar free convection in triangular enclosures. *Int. J. Heat Mass Transfer*, Vol. 25, 991–998.

Asan, H. & Namli, L. (2002). Numerical simulation of buoyant flow in a roof of triangular cross-section under winter day boundary conditions. *Energy Buildings*, Vol. 33, 753–757.

Asan, H. & Namli, L. (2000). Laminar natural convection in a pitched roof of triangular cross-section: Summer day boundary conditions. *Energy Buildings*, Vol. 33, 69–73.

Del Campo, E. M., Sen, M. & Ramos, E. (1988) Analysis of laminar natural convection in a triangular enclosure. *Numer. Heat Transfer.*, Vol. 13, 353–372.

Farrow, D. E. & Patterson, J. C. (1993). On the response of a reservoir sidearm to diurnal heating and cooling. *J. Fluid Mech.*, Vol. 246, 143–161.

Flack, R. D. (1980) The experimental measurement of natural convection heat transfer in triangular enclosures heated or cooled from below, *Trans. ASME: J. Heat Transfer*, Vol. 102, 770–772.

Flack, R. D. (1979) Velocity measurements in two natural convection air flows using a laser velocimeter. *Trans. ASME: J. Heat Transfer*, Vol. 101, 256–260.

Haese, P. M. & Teubner, M. D. (2002). Heat exchange in an attic space. *Int. J. Heat Mass Transfer*, Vol. 45, 4925–4936.

Holtzmann, G. A., Hill, R. W. & Ball, K. S. (2006). Laminar natural convection in isosceles triangular enclosures heated from below and symmetrically cooled from above. *Trans. ASME: J. Heat Transfer*, Vol. 122, 485–491.

Hyun, J. M. (1994). Unsteady buoyant convection in an enclosure. *Adv. Heat Transfe*, Vol. 24, 277–320.

Kent, E. F. (2009a) Numerical analysis of laminar natural convection in isosceles triangular enclosures. *Proceedings of the Institution of Mechanical Engineers Part C - Journal of Mechanical Engineering Science*, Vol. 223, 1157–1169.

Kent, E. F. (2009b). Numerical analysis of laminar natural convection in isosceles triangular enclosures for cold base and hot inclined walls. *Mechanics Research Communications*, Vol. 36, 497–508.

Kent, E. F., Asmaz, E. & Ozerbay, S. (2007). Unsteady natural convection in a water-filled isosceles triangular enclosure heated from below. *Int. J. Heat Mass Transfer*, Vol. 44, 187–200.

Leonard, B. P. & Mokhtari, S. (1990). ULTRA-SHARP Nonoscillatory Convection Schemes for High-Speed Steady Multidimensional Flow. *NASA Lewis Research Centre*, NASA TM 1-2568 (ICOMP-90-12).

Ostrach, S. (1988). Natural convection in enclosures. *Trans. ASME: J. Heat Transfer*, Vol. 110, 1175–1190.

Poulikakos, D. & Bejan, A. (1983a) Natural convection experiments in a triangular enclosure. *Trans. ASME: J. Heat Transfer*, Vol. 105, 652–655.

Poulikakos, D. & Bejan, A. (1983b) The fluid dynamics of an attic space. *J. Fluid Mech.*, Vol. 131, 251–269.

Ridouane, E. H., Campo, A. & Hasnaoui, M. (2006) Benefits derivable from connecting the bottom and top walls of attic enclosures with insulated vertical side walls. *Numer. Heat Trans. Part A-Applications*, Vol. 49, 175–193.

Ridouane, E. H. & Campo, A. (2006). Formation of a pitchfork bifurcation in thermal convection flow inside an isosceles triangular cavity. *Physics of Fluids*, Vol. 18, 074102.

Ridouane, E. H., Campo, A. & McGarry, M. (2005) Numerical computation of buoyant airflows confined to attic spaces under opposing hot and cold wall conditions. *Int. J. Therm. Sci.*, Vol. 44, 944–952.

Saha, S. C. (2011a). Unsteady natural convection in a triangular enclosure under isothermal heating. *Energy Buildings*, Vol. 43, 701–709.

Saha, S. C. (2011b). Scaling of free convection heat transfer in a triangular cavity for Pr > 1. *Energy Buildings*, under review.

Saha, S. C., Patterson, J. C. & Lei, C. (2010a). Natural convection in attics subject to instantaneous and ramp cooling boundary conditions. *Energy Buildings*, Vol. 42, 1192–1204.

Saha, S. C., Patterson, J. C. & Lei, C. (2010b).Natural convection and heat transfer in attics subject to periodic thermal forcing. *Int. J. Therm. Sci.*, Vol. 49, 1899–1910.

Saha, S. C., Patterson, J. C. & Lei, C. (2010c). Natural convection in attic-shaped spaces subject to sudden and ramp heating boundary conditions. *Heat Mass Transfer*, Vol. 46, 621–638.

Saha, S. C. (2008). Natural convection in attics subject to instantaneous and ramp cooling boundary conditions. *PhD Thesis*, School of Engineering and Physical Sciences, James Cook University.

Saha, S. C., Lei, C. & Patterson, J. C. (2007). Effect of aspect ratio on natural convection in attics subject to periodic thermal forcing. *ANZIAM J.*, Vol. 48, C677–C691.

Salmun H. (1995a). Convection patterns in a triangular domain. *Intl. J. Heat Mass Transfer.*, Vol. 18, 351–362.

Salmun H. (1995b). The stability of a single-cell steady-state solution in a triangular enclosure. *Intl. J. Heat Mass Transfer.*, Vol. 18, 363–369.

Convection and Conduction Heat Transfer

Edited by Dr. Amimul Ahsan

ISBN 978-953-307-582-2
Hard cover, 394 pages
Publisher InTech
Published online 17, October, 2011
Published in print edition October, 2011

The convection and conduction heat transfer, thermal conductivity, and phase transformations are significant issues in a design of wide range of industrial processes and devices. This book includes 18 advanced and revised contributions, and it covers mainly (1) heat convection, (2) heat conduction, and (3) heat transfer analysis. The first section introduces mixed convection studies on inclined channels, double diffusive coupling, and on lid driven trapezoidal cavity, forced natural convection through a roof, convection on non-isothermal jet oscillations, unsteady pulsed flow, and hydromagnetic flow with thermal radiation. The second section covers heat conduction in capillary porous bodies and in structures made of functionally graded materials, integral transforms for heat conduction problems, non-linear radiative-conductive heat transfer, thermal conductivity of gas diffusion layers and multi-component natural systems, thermal behavior of the ink, primer and paint, heating in biothermal systems, and RBF finite difference approach in heat conduction. The third section includes heat transfer analysis of reinforced concrete beam, modeling of heat transfer and phase transformations, boundary conditions-surface heat flux and temperature, simulation of phase change materials, and finite element methods of factorial design. The advanced idea and information described here will be fruitful for the readers to find a sustainable solution in an industrialized society.

INTECH
open science | open minds

InTech Europe
University Campus STeP Ri
Slavka Krautzeka 83/A
51000 Rijeka, Croatia
Phone: +385 (51) 770 447
Fax: +385 (51) 686 166
www.intechopen.com

InTech China
Unit 405, Office Block, Hotel Equatorial Shanghai
No.65, Yan An Road (West), Shanghai, 200040, China
中国上海市延安西路65号上海国际贵都大饭店办公楼405单元
Phone: +86-21-62489820
Fax: +86-21-62489821

IntechOpen